# Final Technical Report

# Award Number: G12AP20046

# Episodic and Steady Strain Changes along the Cholame Segment of the San Andreas Fault

Duncan Carr Agnew
Institute of Geophysics and Planetary Physics
Scripps Institution of Oceanography
University of California
La Jolla CA 92093-0225 USA
(858) 534-2590 (FAX 534-5332)
dagnew@ucsd.edu Start and End Dates:

March 1, 2012 to August 31, 2013

February 1, 2014

**Abstract**

This grant supported the analysis of strainmeter and other data on the Cholame segment of the San Andreas fault, just southeast of the Parkfield region. We find that:

1. Remeasurement of a fault-crossing geodetic array shows that over the last 41 years there has been a creep rate of 2.1 mm/yr across the San Andreas fault.
2. Continuous GPS stations 1 km apart and spanning the same part of the San Andreas fault show an average (and steady) creep rate of 2.8 mm/yr over the last 6 years.
3. A comparison of the data from one of the PBO long-base strainmeters (LSM) with GPS measurements over a parallel but longer line show that the LSM is measuring strain changes out to periods of years, including secular strain accumulation.
4. The two PBO strainmeters, after correcting for rainfall effects, show evidence of a strain transient in 2010, lasting for 6 to 9 months.
5. At the beginning of this long-period transient, a day-long transient occurred, with a different signature; modeling shows that this has to have been in the upper few km of the fault zone, probably within the creeping region.

# 1 Introduction

The purpose of this project was to analyze deformation data along the Cholame segment of the San Andreas fault to improve our understanding of strain changes caused by slip on this segment, most especially rapid and apparently aseismic variations seen in the summer of 2010. In contrast to the Parkfield region just to the northwest, this region is nearly aseismic and has very little creep across the surface trace of the San Andreas. This is assumed to occur because the fault changes from creeping to locked behavior here. This area is also believed to be near the initiation point of the last great earthquake on the southern San Andreas, in 1857 (Agnew and Sieh, 1978; Sieh, 1978a).

## 1.1 The Regional Setting

The northern end of the southern San Andreas fault is generally taken to be about where the fault crosses Highway 46, at the southern end of the Cholame Valley. As the top panel in **Figure 2** makes clear, this location coincides with a stepover that is, over 200 km of the fault, the only large offset (Simpson *et al.*, 2006).

Other data summarized in **Figure 2**, show that many changes in fault behavior occur at this stepover. To the northwest, small earthquakes happen at a fairly steady rate, punctuated at Parkfield by a magnitude 6 event every few decades; even farther to the northwest, in the creeping section, there are no large events at all. Paleoseismic data show that slip in the 1857 earthquake was about 5 m to the southeast of Highway 46, falling to much smaller values to the northwest (Sieh, 1978b; Lienkaemper, 2001; Toke *et al.*, 2006). To the southeast, the fault is (now) nearly aseismic. Measurements of surface creep along the fault also change in this region: a rate of about 25 mm/yr in the "creeping section" (Titus *et al.*, 2006), decreases from a point about 50 km northwest of Highway 46 to a small value at Highway 46, and is generally thought to be zero farther to the southeast. Measurements of interseismic motion, mostly from northwest of Highway 46, have been inverted by Segall and Harris (1987), Murray and Segall (2001) and Murray and Langbein (2006) in terms of spatially variable slip on the SAF; Murray and Langbein find that southeast of the 25 km point in **Figure 2** the interseismic slip above 15 km is only a few mm/yr, and set it to zero (fully locked fault) at about −10 km – though given their data distribution, the model resolution is poor in this region. All these patterns were just clear enough 45 years ago for Allen (1968) to propose that Cholame marked a point of transition between two types of fault behavior, an idea that has held up remarkably well.

As Toke and Arrowsmith (2006) point out, the slip deficit in the Cholame segment is now close to the slip released in 1857; on the basis of foreshock reports, it is possible that the 1857 earthquake initiated in this region. Obviously the fault south of Highway 46 is thus

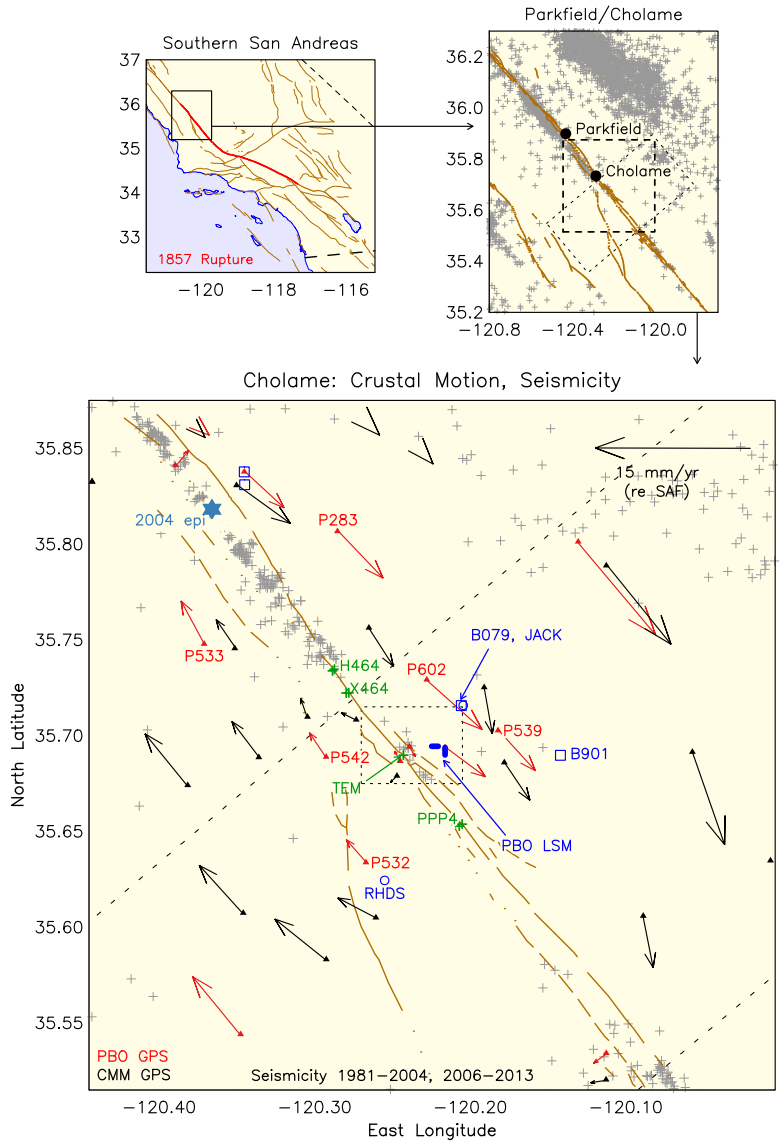


Figure 1: The upper left and right panels show the location of the Cholame region. The heavy dashed box on the right panel shows the area covered by the bottom panel, which shows the San Andreas Fault (brown) in the Cholame area. The black and red arrows are long-term motions relative to the average of GPS sites P552 and P578, located athwart the trace of the San Andreas (see **Figure 4** and **Figure 5**); red is from PBO, black from SCEC Crustal Motion Map. Green points are alignment arrays across SAF, blue lines the two PBO laser strainmeters, blue squares the PBO borehole strainmeters, and blue circles borehole dilatometers installed by the USGS. The blue star is the epicenter of the 2004 Parkfield earthquake; the 1966 epicenter is to the northwest of the area shown here. Seismicity is from 1981 to just before the 2004 event, and from 2006 onwards. In this panel the dotted rectangle shows the location of **Figure 4**; the two diagonal lines, like the light dashed rectangle in the upper right panel, show the area examined in **Figure 7**.

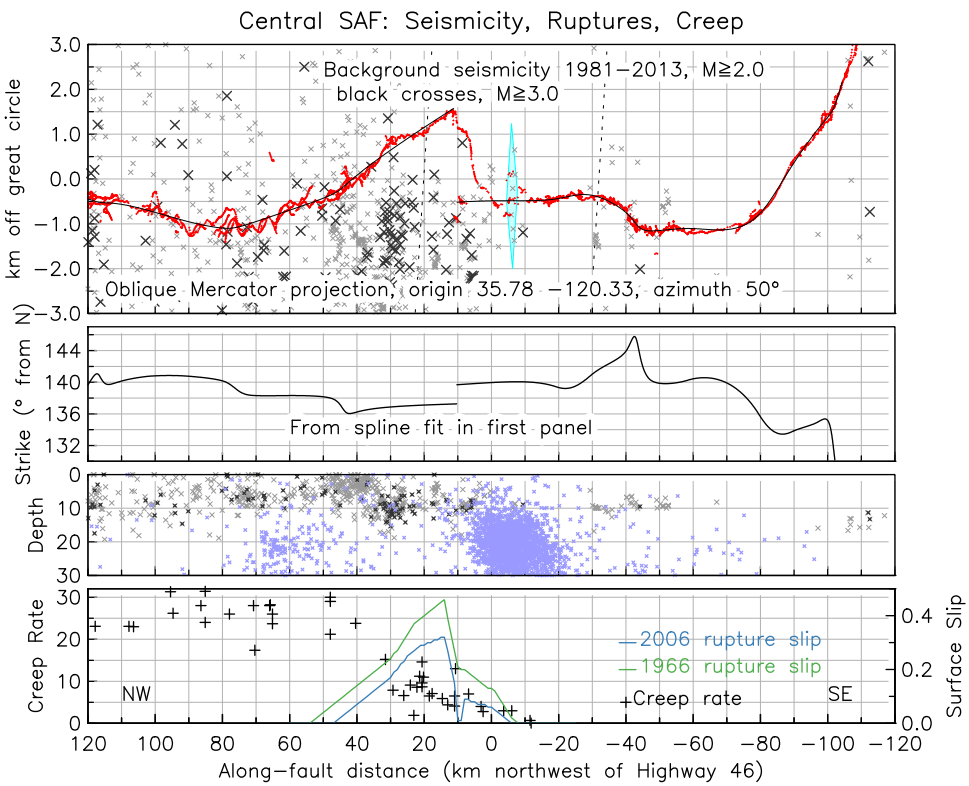


Figure 2: Along-fault variations around the Cholame area; in all cases the $x$-coordinate is distance along a great circle nearly along the fault trace, with the origin at the point where the fault crosses Highway 46. The top panel (cross-fault scale much exaggerated) plots the seismicity (gray and black) and surface trace (red); the black line overlaid on the red is a spline fit to the fault trace. Except for the stepover at Highway 46, the mapped trace matches the spline fit to within 100 m or less, over a total distance of over 200 km. The nearly vertical dashed lines show the north and south boundaries of **Figure 1**, and the blue polygon the region covered by **Figure 5**. The second panel shows the fault strike derived from the spline fit, and the third shows a cross-section of the seismicity, with tremor locations (Nadeau and Guilhem (2009), updated through 2013) in blue. The bottom panel shows coseismic surface slip for the 1966 and 2004 earthquakes (Toke *et al.*, 2006), and interseismic surface creep rates (Bennett, 1979; Burford and Harsh, 1980; Baker, 1993; Titus *et al.*, 2006).

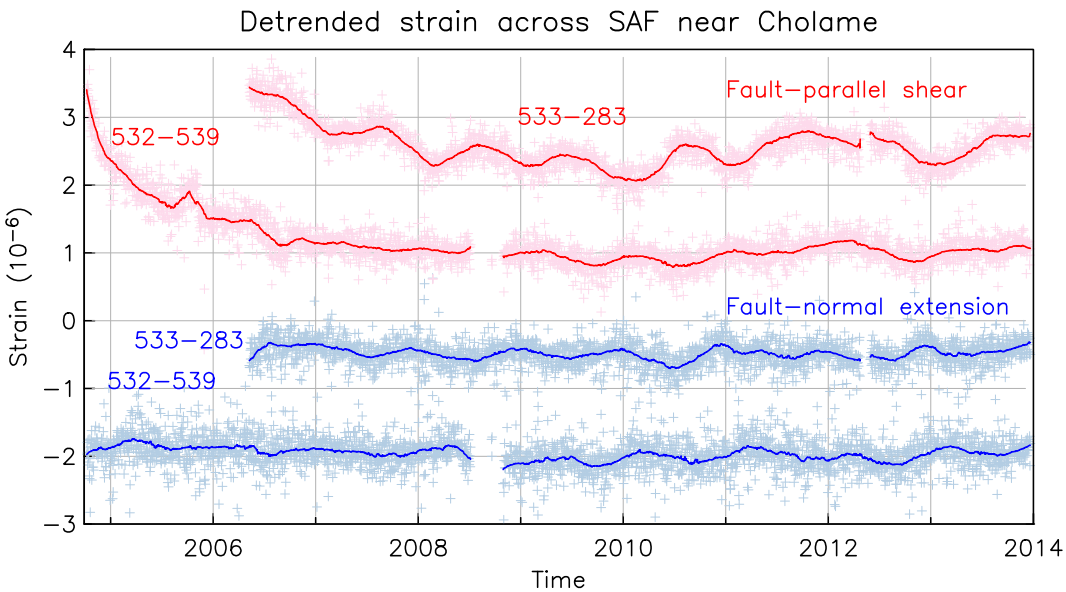


Figure 3: Fault-parallel and fault-normal motion (after detrending) between pairs of GPS sites (see **Figure 1** for locations) computed from the PBO time series. Long-term trends were determined using data from 2007 on and subtracted. The solid lines are smoothed from the daily values (crosses). Long-term rates for 533-283 are $-2.52 \times 10^{-6}$/yr in shear, and $0.12 \times 10^{-6}$/yr in extension. Long-term rates for 532-539 are $-1.91 \times 10^{-6}$/yr in shear, and $0.05 \times 10^{-6}$/yr in extension. Note that the latter series begins just after the 2004 Parkfield earthquake.

of special interest. But most investigations have focused on the partly-creeping area to the northwest. One reason for this was the Parkfield earthquake prediction (Roeloffs and Langbein, 1994), which gave rise to an intense monitoring program; more recently the SAFOD project, drilling though a part of the fault with abundant shallow seismicity, has also drawn attention to this northern region.

More recently, Nadeau and Dolenc (2005) showed evidence for very unusual signals from the fault south of Cholame: "tremor" signals that are similar to those seen as part of the Episodic Tremor and Slip phenomenon in Cascadia. This tremor appears to be much deeper (35 km) than the earthquake seismicity along this part of the fault, and its behavior – and still more its causes – remain enigmatic. Initial searches for associated deformation did not show any short-term dilatation associated at the times of the tremor Johnston *et al.* (2006); it was in large part to improve the detection of possible aseismic deformations that the PBO Steering Committee recommended that a pair of long-base laser strainmeters be installed in the Cholame area. To provide additional information near this strainmeter pair, PBO installed four additional continuous GPS stations nearby, densifying the network of continuous GPS stations already installed, most of them soon after the 2004 Parkfield earthquake. **Figure 3** shows the time series from the two GPS sites that give long lines crossing the fault in the Cholame area; these show that the rate of shear across the fault,

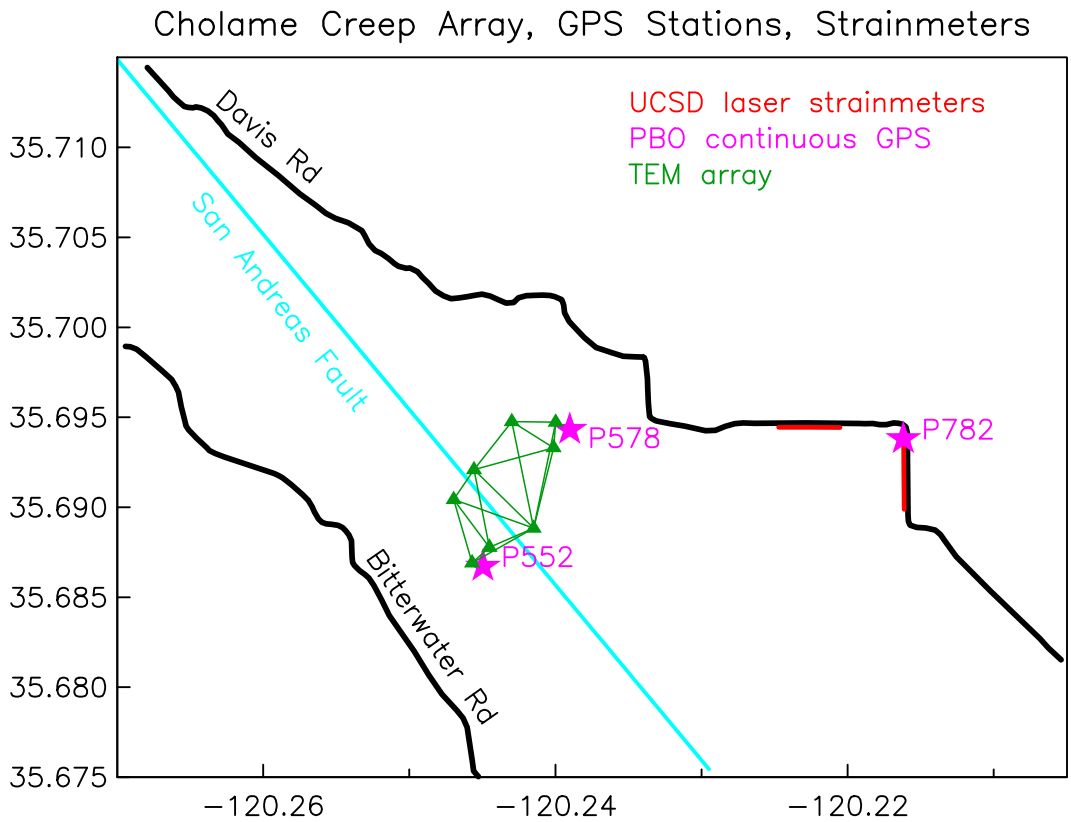


Figure 4: Detail map of the area adjacent to the Cholame laser strainmeters (LSM's) and the San Andreas fault, showing the NGS network set up to monitor fault creep, the three PBO GPS sites, and the LSM's. PBO site P782 is mounted on the North end building of the NS LSM.

while affected by time-varying deformation after the Parkfield earthquake (Freed, 2007), returned to a steady rate by 2008.

# 2 Work Plan and Results

This section describes our investigations in three areas: creep over long and short times on this section of the fault; strain close to the fault as measured by strainmeters and GPS over the last few years; and rapid aseismic signals that appear to reflect a creep event at relatively shallow depth.

This range of investigations is possible because of a fortuitous confluence of geodetic monitoring methods in a single small part of the fault, in the small dashed box in **Figure 1**, shown in more detail in **Figure 4**.

When the California Aqueduct was originally planned in the early 1960's, one branch of it was intended to cross the San Andreas fault in the Cholame region; and here, as at other planned crossings the U.S. Coast and Geodetic Survey[1] installed a small array of monuments to monitor possible future fault motion. This particular array was called the "TEM" array, and consisted of four monuments forming a fault-crossing quadrilateral, with an additional four extending the array over a slightly larger region, so that the entire array covered about 1 km across the fault.

Part of the PBO siting plan called for the construction of a pair of longbase laser strainmeters in the Cholame area; the end result of our search for a site, involving logistical and landowner issues, was a pair of instruments along Davis Road, relatively close to the San Andreas fault. In order to complement the LSM measurements by densifying the continuous GPS network, PBO engineer Chris Walls installed five additional sites, three of which are shown on **Figure 4**. P552 and P578 are standard PBO installations with drilled braced monuments, while P782 is an antenna mounted on the roof of the North instrument building of the NS LSM. Entirely by chance, P552 and P578 are each close to the ends of the NGS fault-crossing array, 1.001 km apart.

## 2.1 Creep from Decades to Years

The TEM array of monuments, shown in more detail in **Figure 5**, was surveyed by NGS, using triangulation between all intervisible marks, and one taped distance. This was done in 1964, 1965, and 1966 (following the Parkfield earthquake); NGS made trilateration surveys in 1968 and 1971. Monitoring was turned over to the California Division of Mines and Geology, which made further trilateration surveys of the main fault-crossing lines in 1978 (Bennett, 1979).

Fortunately, as **Figure 5** shows, this array is entirely on privately-owned ranch land, which has not been developed in the 50 years since the array was constructed. It is thus, unlike many of the other fault-crossing arrays, perfectly preserved. Clearly, a resurvey of this array could provide a very precise estimate of the long-term creep on this part of the San Andreas fault, over an even longer interval than was possible for the resurveys described by Titus *et al.* (2006). We therefore (with travel funds from the Marine Science Committee on Research of the UC San Diego Academic Senate) made a full resurvey of this array on October 17-18, 2012, occupying the marks with geodetic GPS receivers for 6 to 24 hours. We processed these data, along with the data from the three PBO sites in **Figure 4**, using the GAMIT processing package. Because of the short lengths of the lines, we used the L1 frequency only.

The simplest comparison is with the line-lengths measured in 1971 by the NGS, since these

[1] As the National Geodetic Survey was then called.

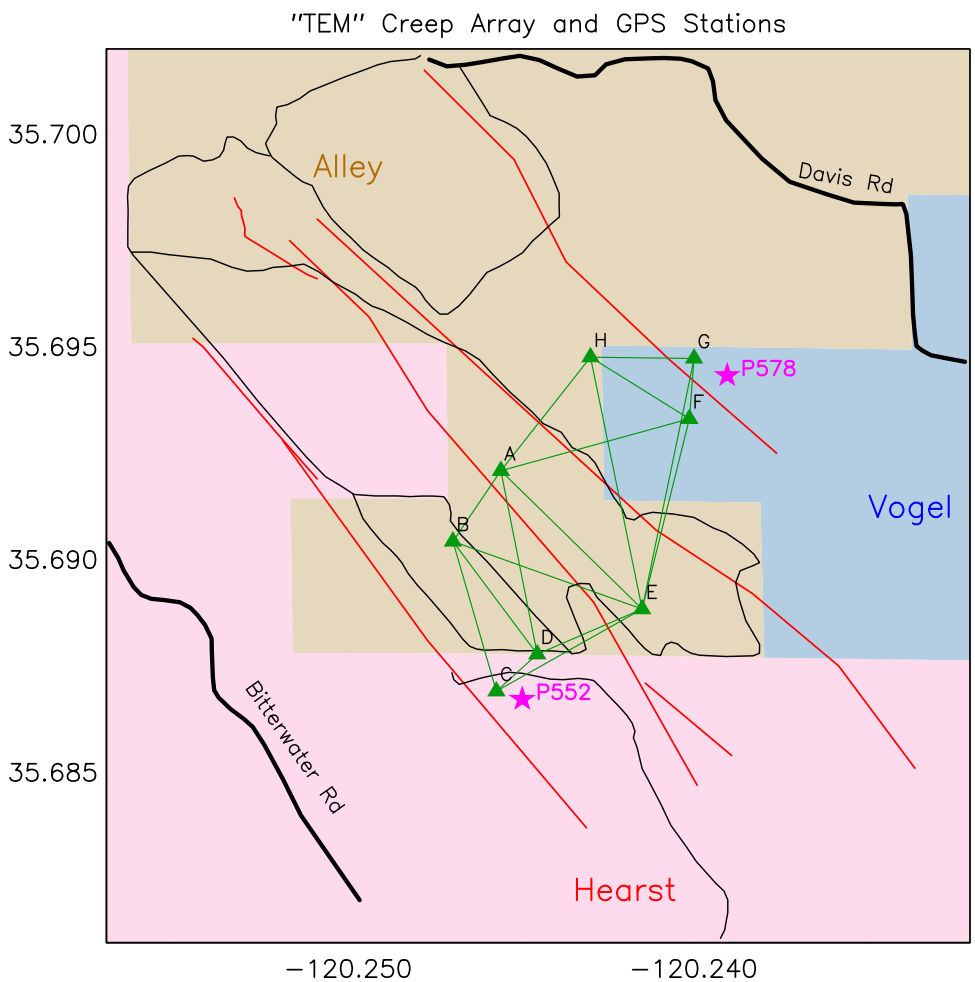


Figure 5: Detail of the NGS "TEM" array, with monument labels shown, along with landownership. Heavy black lines are paved roads, and lighter lines ranch roads. Red lines are mapped fault traces.

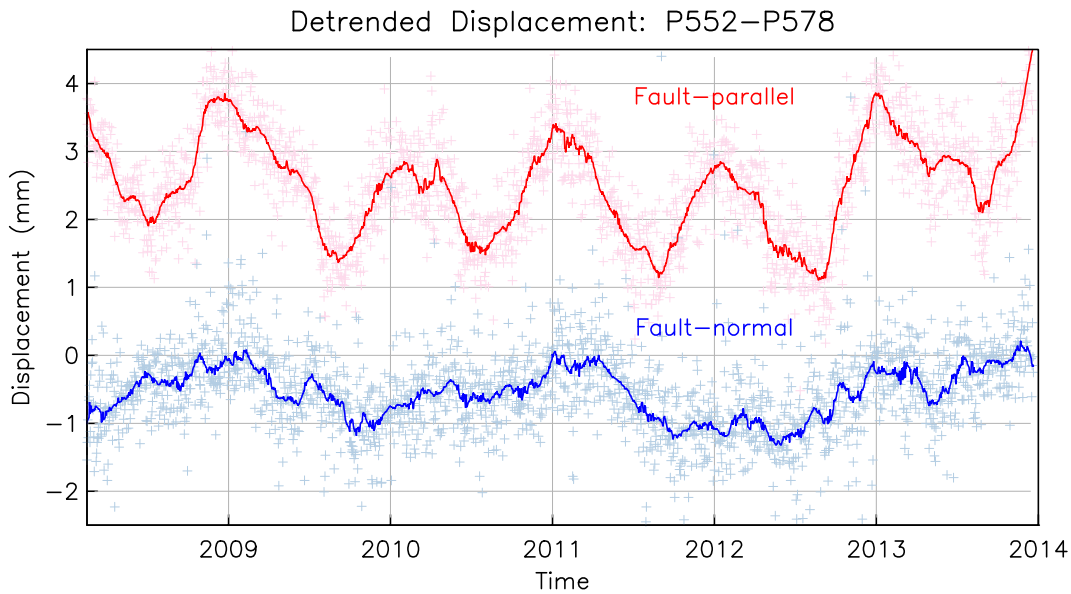


Figure 6: Fault-parallel and fault-normal motion between pairs of GPS sites (see **Figure 5** for locations) computed from the PBO time series, after removing long-term trends. The solid lines are smoothed from the daily values (crosses). The long-term trends subtracted are 2.82 mm/yr fault-parallel, and −0.19 mm/yr fault-normal.

are available as mark-to-mark distances[2]. Only three line lengths show changes greater than 11 mm: A-D has shortened by 93 mm, B-E has lengthened by 84 mm, and A-H has lengthened by 35 mm. Except perhaps for the last change, all the measurements are consistent with all motion taking place inside the ABDE quadrilateral, with right-lateral creep of 88 mm, for a 41-year creep rate of 2.1 mm/yr.

Since both ends of the TEM array lie very close to continuous GPS stations run by PBO (**Figure 5**) we can compare this long-term rate to what these sites have recorded over the last six years. We have processed the data independently of the PBO processing centers, using, for this short baseline, the LC observable but with no zenith delay estimation[3]. This gave very low scatter – but, somewhat surprisingly, not better results (except in the vertical) than could be obtained by differencing the PBO time series[4]; **Figure 6** shows the results after removing a trend. There are annual cycles present, which may reflect monument motion, although because they are nearly perfectly aligned, like the very local topography, with the fault-parallel direction it is possible that they represent thermoelastic effects (Hill *et al.*, 2009).

[2] We thank Richard Snay for making this information available

[3] We also tried processing with the L1 frequency only, either for 24 hours or for 12 hours at night; the results were not significantly better than those found using LC, unlike the results for a 50-m baseline in Wyatt and Agnew (2004).

[4] Both approaches showed s 3 mm offset (in east and north) in P578 owing to an antenna change on 2008:303.

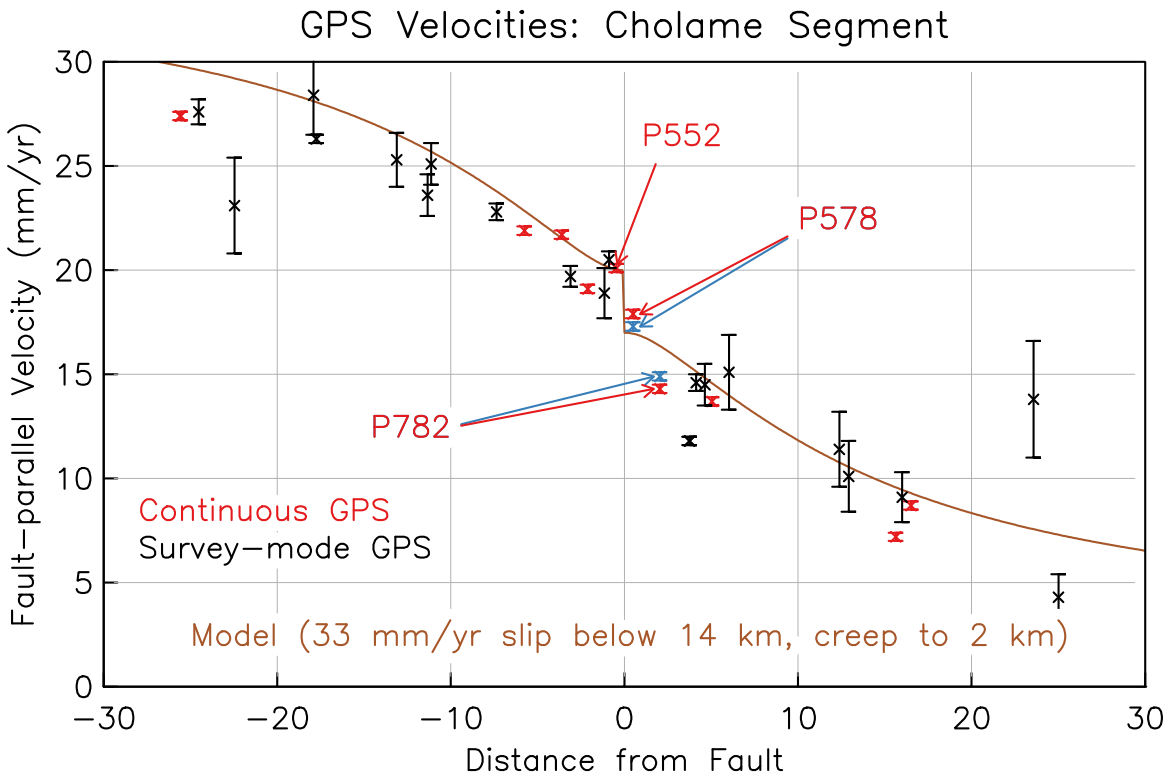


Figure 7: The fault-parallel component of GPS velocities from the Cholame region (northeast-southwest striking box in **Figure 1** taken from the sources described in the caption to that figure, but here referenced to the Sierra-Nevada/Great-Valley microplate using the rotation pole of Titus *et al.* (2011). Two velocities are shown for P578 and P782; the ones in blue are based on the rates shown in **Figure 6** and **Figure 8**, with the PBO velocity assumed for P552. The brown line is a two-dimensional dislocation/crack model of the displacement, assuming slip of 33 mm/yr below 14 km, and a stress-free surface on the fault, with a depth of 2 km.

The creep rate from the resurvey of the TEM array (2.1 mm/yr) and the continuous GPS stations (2.8 mm/yr) differ slightly; this might indicate a more rapid rate in the years following the 2004 Parkfield earthquake, although there is no obvious time dependence in **Figure 6**. The larger value from the continuous GPS may indicate that there is a small amount of additional creep to the NE of the fault-crossing quadrilateral, though the resurvey measurements do not appear to support this. What is clear is that there is creep on this part of the fault, though the amount is much less than the overall slip rate of the fault at depth. So the fault is not entirely locked at this location. deMichele *et al.* (2011) use 11 years of InSAR data to find a creep rate of about 3 mm/yr at this location, decaying to zero about 8 km further to the southeast (see also Lisowski and Prescott (1981)).

We put this result about creep into a wider setting in **Figure 7**, which shows the fault-parallel component of GPS velocities from the Cholame region. Thanks in part to the PBO densification of this area, the pattern of deformation is clear – but its interpretation is not.

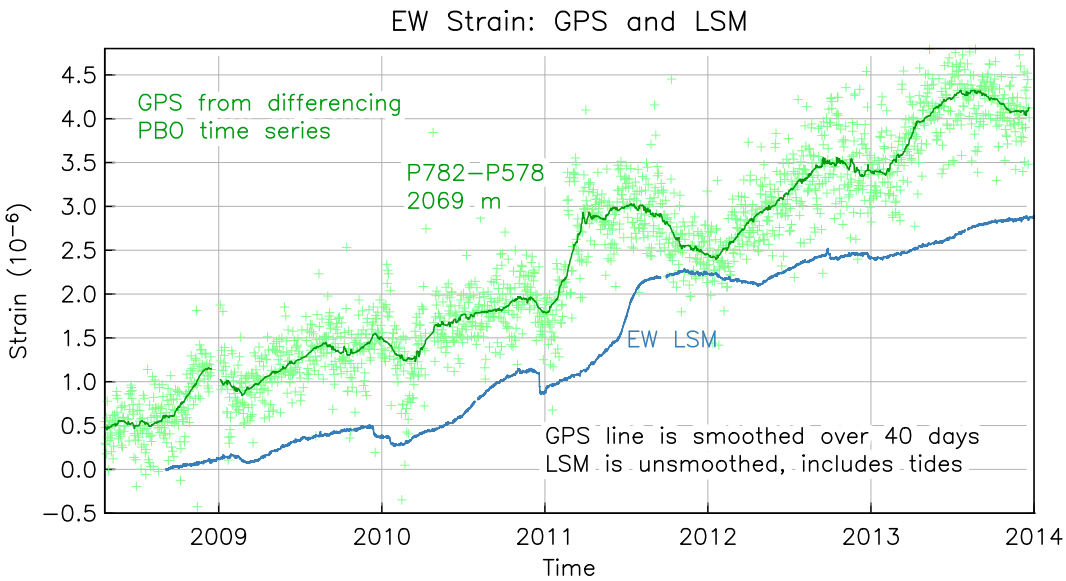


Figure 8: Comparison of the EW strain as estimated from the GPS and from the EW LSM. The GPS data are shown as daily values and a curve smoothed from them.

If no creep is present, this figure could be taken to show that on the two sides of the San Andreas fault the velocity gradients differ significantly, with asymmetric deformation. This has been observed before about the San Andreas fault in this general area, though only over a wider region (Schmalzle *et al.*, 2006), and on other faults (Pichon *et al.*, 2005; Jolivet *et al.*, 2009). However, once we include creep this asymmetry no longer appears to be necessary: **Figure 7** also shows a model in which a dislocation at 14 km depth drives the overall motion, but a shallow stress-free part of the fault relieves the induced stress, causing creep on the fault and a modification of the displacement profile close to it.

## 2.2 Strain Accumulation: LSM Performance and GPS Comparison

Moving slightly farther from the San Andreas fault, we next examine the long-term rates of strain seen on the LSM's at Cholame. We start with a comparison that is possible because of another fortuitous arrangement, namely that the two PBO GPS sites P578 and P782 are on an almost exactly EW line, 2.4 km long, that includes the span of the EW LSM. The length change in the GPS baseline is thus a measure of EW strain that can be compared directly with the EW strainmeter record, though with two caveats:

- Since one end of the GPS line is significantly closer to the San Andreas fault, we would expect some difference in the long-term slip rate.

- The west end of the GPS line is a deep-braced monument, but the east end is the top of a building: the instrument building for the north end of the NS strainmeter. While this building contains an optical-anchor system, this measures only NS motion, not any EW motions that would affect the GPS baseline length.

As **Figure 8** shows, the long-term (secular) strain found from both systems is in good agreement: a most rewarding result, since it confirms that the LSM is capable of recording secular deformation, something not possible with borehole strainmeters – or, indeed, any other type of strainmeter we are aware of. The agreement is not perfect, since the GPS strain appears to show a slight, but significant, change in rate after 2010, while the LSM does not.

It is tempting to look at the smoothed GPS in **Figure 8** and view it as equivalent to the LSM – but this view is illusory and the temptation should be resisted. The GPS can be made as smooth-looking as the LSM only by heavy averaging, in this case over a timespan of 0.1 yr; on time scales of days the true GPS variation is much larger, as shown by the scatter of the daily estimates. And at shorter periods the strainmeter noise level is so much snaller that it is much less than the thickness of the line. So the LSM provides the lowest possible noise over the widest range of frequencies.

With this GPS-LSM comparison available to bolster the reality of the longest-period variations in the LSM data, what do these data show? We believe that they provide good evidence for a long-term strain event, seen on both LSM's, that extended over the last six months of 2010 and into 2001. At these very long periods the Cholame LSM records are influenced by episodes of sustained rainfall; fortunately, most of the induced strain changes can be modeled and then removed from the records. This is possible because over time the response decays with time. The records show a threshold effect, with no response to light rains, presumably because these are absorbed by near-surface soils and do not affect the water content at greater depths. Above this threshold a simple impulse response, scaled by the amount of rain, seems to match much of the variation in the data.

**Figure 9** shows how we have used this model to remove the rain-related signal. Beginning with the strains corrected for recorded endpoint motion, we first remove a trend and an annual cycle, determined from the data before 2010. We then take the rainfall affecting each instrument, which involves different (but consistent) thresholds for each instrument. This is to be expected, since the displacements are most likely caused by wetting and drying of regolith material at depths comparable to the anchoring depth of the strainmeters (20 m); and this wetting and drying involves not just the amount of water hitting the ground, but also how much runs off, is evaporated, or taken up by plants, rather than penetrating to depth.

We then convolve the rain series (after removing the smaller changes) with a single impulse response, and subtract this to get the fully corrected strain. The extremely heavy rains at the end of 2010 caused additional strain changes, not entirely corrected by the model. But a

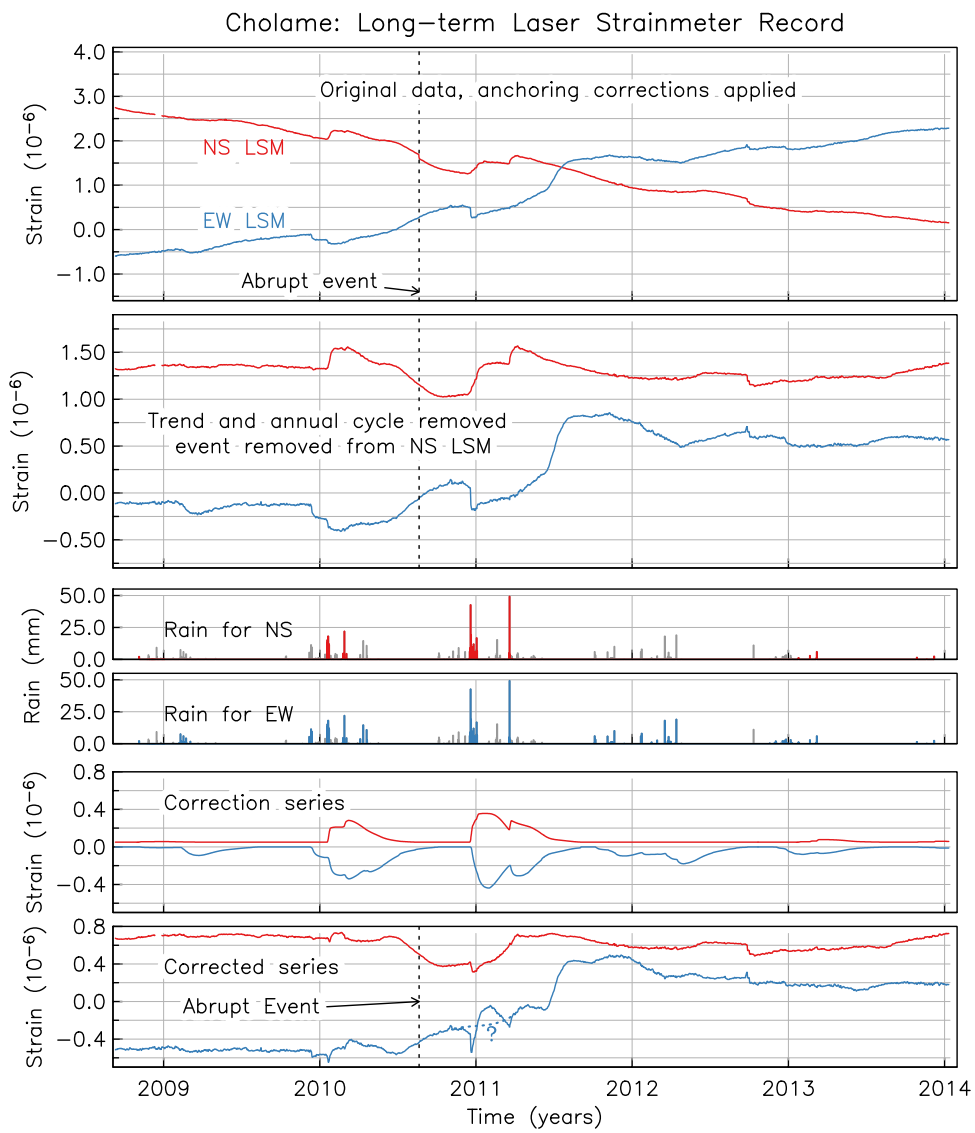


Figure 9: Strain from the two PBO strainmeters at Cholame. The top panel shows the strain data, and the next panel the same after subtracting an trend and annual cycle, both found for the data before 2010. The next two panels (with an expanded scale) show the daily rainfall, colored if above the threshold for causing a signal on the strainmeter, and gray if not. The fifth panel shows the result of convolving this with an impulse response estimated using the data before 2011, and the sixth panel shows the residual. Most of the rain-related signals have been substantially reduced, leaving only a transient on the NS strain from mid-2010 to early 2011, and a step transient in the EW from mid-2010 to mid-2011. Note that the rate after mid-2011 is comparable to that before mid-2010 on both systems. The transient on 2010:232 has been removed from the NS strain on all but the first plot. The rate on the NS LSM is $-0.46 \times 10^{-6}$/yr; the annual cycle is $54 \times 10^{-9}$ with phase 167° relative to January 1. The rate on the EW LSM is $0.42 \times 10^{-6}$/yr; the annual cycle is $16 \times 10^{-9}$ with phase 146°.

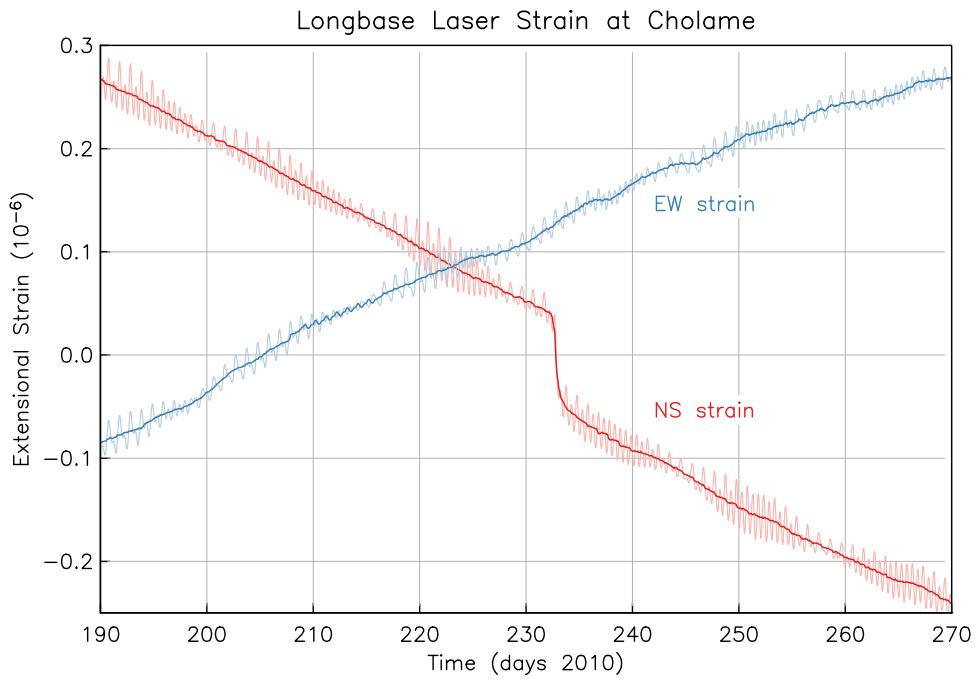


Figure 10: Strain event as recorded on the longbase laser strainmeters in Cholame. Both series have had predicted tides removed, along with pressure corrections and a diurnal cycle caused by uncompensated temperature effects. The secular trend has *not* been removed.

long-term change in strain is evident in both series, with the event on 2010:233 (discussed in the next section) being near the start of this. The short-term and long-term variations have different signatures; in particular, the short-term change is completely absent from the EW record, while the long-term change is largest on this component – and appears to take the form of a step change, with very similar long-term rates before and after (remembering that the long-term rate was derived only from data before 2010).

## 2.3 Aseismic Strain Events

As described in Section 2.2, from the time the two laser strainmeters in Cholame began operation (September 4, 2008, or 2008:248), they have shown secular changes consistent with the expected strain near the fault, but initially displayed no time variations from tectonic sources. This changed at 2010:232:07 (August 20), when the NS instrument began to show an anomalously rapid contraction (**Figure 10**). Since the EW instrument showed no rapid changes, we initially believed that this reflected an instrumental problem, but thorough checks failed to reveal any. The change on the NS ended after 39 hours, still with no detectable change seen on the EW instrument.

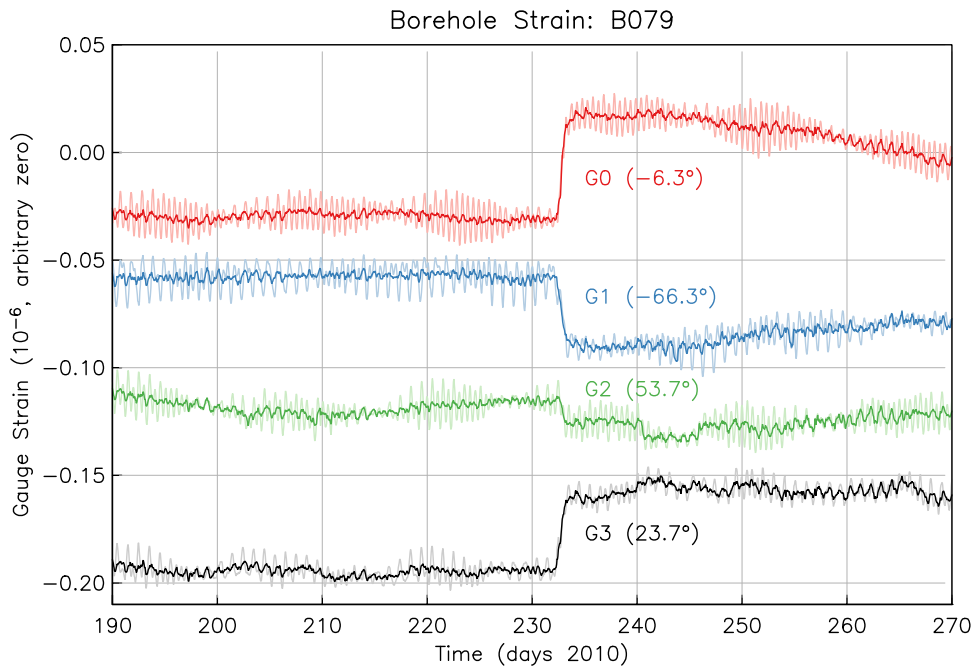


Figure 11: Strain event as recorded on borehole strainmeter B079; the units are nominal strain on each of the GTSM gauges, not corrected for borehole effects. For all series the predicted tides were removed, along with the effects of air pressure, a diurnal cycle, and an exponential fit to the whole series, followed by local detrending.

Had this signal been seen on only the NS strainmeter, we would have assumed that it was indeed an instrument problem, since we would normally expect any tectonic signal to appear on both instruments – tidal data and secular strain rates show that both are well coupled to the Earth. But a signal with similar form was observed at the same time on the PBO borehole strainmeter B079, located 2.6 km from the laser strainmeters (**Figure 1**) and also, more weakly, on borehole strainmeter B901, 6.7 km to the east (Hodgkinson *et al.*, 2013). The signal is very obvious on three of the four BSM gauges at B079; while it is apparent on the fourth (G2), this gauge frequently shows offsets of a similar magnitude that, not being seen on the other gauges, must be spurious. It is therefore unclear how much the data from this gauge can be relied upon for the strain event.

One nontectonic source of simultaneous signals that always needs to be considered is weather; but the environmental data collected at the laser strainmeter site shows nothing more than the hot cloudless days typical of central California in the summer, with no rain for the previous 100 days, and none to come for another month.

### 2.3.1 Inversion for Fault Slip

Given these data, it is clearly important to invert for slip on the fault (assuming this to be the source of the signals). The first step is to find the Green function for observed strains or displacements, given slip at a point on the fault plane. For the $i$-th observable, we write this as $\mathbf{G}_i(x_1, x_2) = \mathbf{G}_i(\mathbf{x})$, where $x_1$ and $x_2$ are the horizontal and vertical coordinates along the fault plane, and $\mathbf{x}$ is the corresponding vector. $\mathbf{G}_i$ itself is a vector; the amount of strain or displacement $\epsilon$ produced as a function of time by slip $\mathbf{s}$ on the fault plane (also vector-valued) is given by a surface integral over the fault plane $P$:

$$\epsilon_i(t) = \int_P \mathbf{G}_i(\mathbf{x}) \cdot \mathbf{s}(\mathbf{x}, t)\, dA \tag{1}$$

Since the individual components of $\mathbf{G}_i$ take on a wide range of values, both positive and negative, over the fault surface $P$, determining $\mathbf{s}(\mathbf{x}, t)$ from a single time series $\epsilon_i(t)$ is impossible: a wide range of slip patterns could produce the same change in observed strain. Even though we have multiple such series, the inversion will remain nonunique, but with additional (and reasonable) assumptions we can form an estimate of the possible slip distribution.

The main assumptions are three:

1. We assume that $\mathbf{s}$ is in fact a scalar, with only one nonzero component $s$: we choose this to be the strike-slip motion.
2. We assume that $s$ is non-negative for all $\mathbf{x}$ and $t$: that is, that the fault slips only in one direction (in this case right-lateral).
3. We assume that for any value of $t$, $s$ is nonzero over a region small enough that $\mathbf{G}_i$ is nearly constant over it; in effect, that $s(\mathbf{x}(t), t) = s(t)\delta(\mathbf{x} - \mathbf{x}_s(t))$ so that the integral becomes a multiplication, making equation (1) into

$$\epsilon_i(t) = G_i(\mathbf{x}_s(t))s(t) \tag{2}$$

where we have made the location of the slip $\mathbf{x}_s(t)$. This reduction of the integral to a multiplication will also be the case if the area being integrated over is of a fixed size and shape, though in that case the slip becomes the average slip over the area.

Since there is no zero level in the observed strain, it is best to work with the time derivative of the signal; we assume that the change in $\mathbf{x}_s$ is slow enough that we need not include it explicitly, in which case equation (2) becomes

$$\dot{\epsilon}_i(t) = G_i(\mathbf{x}_s(t))\dot{s}(t) \tag{3}$$

We now rearrange both the observational and theoretical quantities to give an expression in which the slip amount is decoupled from the Green functions. For $n$ observations define two $n$-vectors $\mathbf{g}$ and $\mathbf{e}$, with the $i$-th component of each one being $g_i = G_i$ and $e_i = \dot{\epsilon}_i$, and define the unit vectors $\mathbf{n}_g = \mathbf{g}/|\mathbf{g}|$ and $\mathbf{n}_e = \mathbf{e}/|\mathbf{e}|$. Then equation (3), applied to all the observations, becomes

$$\mathbf{e}(t) = \mathbf{n}_g(\mathbf{x}(t))\dot{s}(t) \tag{4}$$

The direction of $\mathbf{n}_g$ depends on the ratios of the Green functions $\mathbf{G}_i$, which are a function only of position on the fault.

The method of analysis is thus to find $\mathbf{n}_e(t)$ from the data, perhaps with errors; this will give an acceptable region on the $n$-dimensional hypersphere. We can then map this region into a region on the fault (usually several regions); the slip must occur in such a region. For a particular location, and direction of $\mathbf{n}_e$, we can solve for the slip as

$$s = \frac{|\mathbf{e}|}{|\mathbf{g}|} \tag{5}$$

Considering for the moment only the data from the laser strainmeters, we have just two observation types; we say that $e_1 = \dot{\epsilon}_{\mathrm{EW}}$ and $e_2 = \dot{\epsilon}_{\mathrm{NS}}$, so that $\mathbf{e}$ and $\mathbf{g}$ are two-dimensional vectors. We can then represent the directions of the unit vectors $\mathbf{n}_g$ and $\mathbf{n}_e$ by a scalar quantity, namely an angle $\theta$, measured counterclockwise from the 1-axis; a distance measure between two unit vectors is the cosine of the angle between them. We use $\theta_e$ for $\theta$ inferred from the data, and $\theta_g$ for $\theta$ computed for different locations on the fault.

This representation suggests a method of displaying all values of $\theta_g(\mathbf{x})$: associating each value of $\theta$ with a color hue (in the hue-saturation-brightness description of colors) since these, like $\theta$, lie on a circle. A location with positive EW strain and no NS strain corresponds to $\theta_g = 0$ (red); a location with zero EW strain and positive NS strain corresponds to $\theta_g = \pi/2$ (green-to-yellow); a location with negative EW strain and zero NS strain corresponds to $\theta_g = \pi$ (light blue) and a location with zero EW strain and negative NS strain corresponds to $\theta_g = 3\pi/2$ (blue changing to purple).

**Figure 12** shows this representation of $\theta_g(\mathbf{x})$ for these two observables, plotted on the plane of the San Andreas fault adjacent to the CHL strainmeters; more precisely, on a vertical surface along the spline curve shown in the top panel of **Figure 2**. The responses were computed from the Okada (1985) formulas for an elastic halfspace, assuming uniform slip of

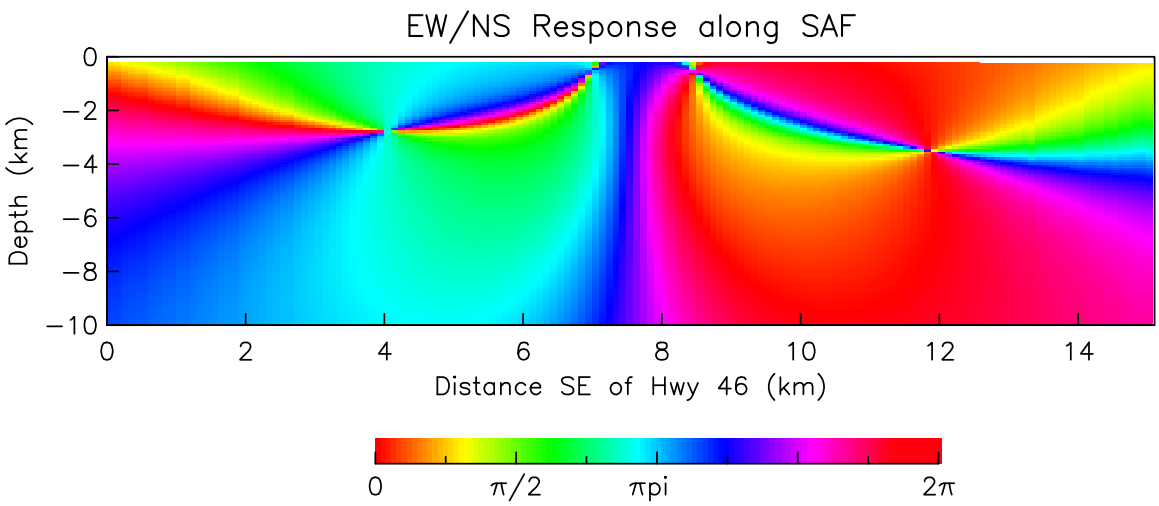


Figure 12: Upper plot shows the relative response of the two LSM's to slip at different locations on the San Andreas fault, using the color-wheel scale shown. The $x$ coordinate is the same one used in **Figure 2**. Note that vertical axis is compressed.

1 cm over a square 100 m on a side. The color bar below the plot shows how different colors correspond to different normalized responses, which are just the sine and cosine of $\theta_g$.

The lack of signal on the EW strainmeter, makes interpreting the laser strainmeter data very straightforward: the slip must have occurred in a color corresponding to zero signal on the EW strainmeter, which in terms of **Figure 12** means a phase close to $\pi/2$: that is, one of the green-to-yellow regions. It could be relatively shallow (0-2 km) and within 4 km of Highway 46; or deeper (about 4 km) and between kilometers 4 and 6; or much further to the southeast (unlikely given the size of the signal on the BSM's).

Including the strain data from the two borehole strainmeters and the upper bound for the displacement given by the GPS data in **Figure 6** would provide additional constraints to be used in the inversion as described above. After differentiating the data to get strain rate, we can combine the strain-rate series to find (in multidimensional space) a direction $\theta_e(t)$ and amplitude $|\mathbf{e}(t)|$; these will have errors that can be estimated from the error in $\dot{\epsilon}$ for each component, which will be a function of the background noise, and will be largest when the signal-to-noise ratio is small. A given range of $\theta_e$ will correspond to a possible range for $\theta_g$, which in turn will correspond to areas of the fault plane. If $\theta_e(t)$ is constant, these areas will be fixed, and the most we can do in an inversion is, for each of them, determine the corresponding time history, $s(t)$, of the slip. If $\theta_e$ varies with time, so will the corresponding areas on the fault plane. It is a reasonable assumption that the slip at any time is spatially contiguous to where it was at the time just previous: this implies that we should prefer locations for which the areas determined by $\theta_e(t)$ do not jump over intervening ones, and preferably move as little as possible,

This type of inversion should give a best-fit result, as well as some indication of the possible range of models for slip associated with the strain event. Work on this more complex inverse problem is in progress.

# References

Agnew, D. C., and K. Sieh (1978), A documentary study of the felt effects of the great California earthquake of 1857, *Bull. Seismol. Soc. Am.*, **68**, 1717–1729.

Allen, C. R. (1968), The tectonic environments of seismically active and inactive areas along the San Andreas fault system, in *Conference on Geologic Problems of the San Andreas Fault System*, edited by W. R. Dickinson and A. Grantz, pp. 70–82, Stanford University, Palo Alto.

Baker, B. (1993), Deformation across the San Andreas fault near Parkfield, California, *M.sc. thesis*, University of Wyoming, Laramie.

Bennett, J. H. (1979), Fault creep measurement, *Calif. Geol.*, **32**, 41–45.

Burford, R. O., and P. W. Harsh (1980), Slip on the San Andreas Fault in central California from alinement array surveys, *Bull. Seismol. Soc. Am.*, **70**, 1233–1261.

deMichele, M., D. Raucoules, F. Rolandone, P. Briole, J. Salichon, A. Lemoine, and H. Aochi (2011), Spatiotemporal evolution of surface creep in the Parkfield region of the San Andreas Fault (1993-2004) from synthetic aperture radar, *Earth and Planetary Science Letters*, **308**, 141–150, doi:10.1016/j.epsl.2011.05.049.

Freed, A. M. (2007), Afterslip (and only afterslip) following the 2004 Parkfield, California, earthquake, *Geophys. Res. Lett.*, **34**, L06,312, doi:10.1029/2006GL029155.

Hill, E., J. L. Davis, P. Elósegui, B. P. Wernicke, E. Malikowski, and N. A. Niemi (2009), Characterization of site-specific GPS errors using a short-baseline network of braced monuments at Yucca Mountain, southern Nevada, *J. Geophys. Res.*, **114**, B11,402, doi: 10.1029/2008JB006027.

Hodgkinson, K. M., D. C. Agnew, F. K. Wyatt, W. Hatfield, D. B. Henderson, D. Mencin, D. Phillips, C. M. Meertens, and G. S. Mattioli (2013), *High-rate strainmeter observations of aseismic creep in a transition zone between creeping and locked sections of the San Andreas fault*, Abstract G32B-05 pp., Amer. Geophys. Union Fall Mtg., San Francisco.

Johnston, M. J. S., R. D. Borcherdt, A. Linde, and M. T. Gladwin (2006), Continuous borehole strain and pore pressure in the near field of the 28 September 2004 M 6.0 Parkfield, California, earthquake: Implications for nucleation, fault response, earthquake prediction, and tremor, *Bull. Seismol. Soc. Am.*, **96**, S56–S72, doi:10.1785/0120050822.

Jolivet, R., R. Burgmann, and N. Houlie (2009), Geodetic exploration of the elastic properties across and within the northern San Andreas Fault zone, *Earth Planet. Sci. Lett.*, **288**, 126–131, doi:10.1016/j.epsl.2009.09.014.

Lienkaemper, J. J. (2001), 1857 slip on the San Andreas fault southeast of Cholame, California, *Bull. Seismol. Soc. Am.*, **91**, 1659–1672.

Lisowski, M., and W. H. Prescott (1981), Short-range distance measurements along the San Andreas Fault system in central California, 1975 to 1979, *Bull. Seismol. Soc. Am.*, **71**, 1607–1624.

Murray, J., and J. Langbein (2006), Slip on the San Andreas fault at Parkfield, California, over two earthquake cycles, and the implications for seismic hazard, *Bull. Seismol. Soc. Am.*, **96**, S283–S303.

Murray, M. H., and P. Segall (2001), Modeling broadscale deformation in northern California and Nevada from plate motions and elastic strain accumulation, *Geophys. Res. Lett.*, **28**, 4315–4318.

Nadeau, R. M., and D. Dolenc (2005), Nonvolcanic tremors deep beneath the San Andreas Fault, *Science*, **307**, 389, doi:10.1126/science.1107142.

Nadeau, R. M., and A. Guilhem (2009), Nonvolcanic tremor evolution and the San Simeon and Parkfield, California earthquakes, *Science*, **325**, 191–193, doi:10.1126/science.1174155.

Okada, Y. (1985), Surface deformation due to shear and tensile faults in a half-space, *Bull. Seismol. Soc. Am.*, **75**, 1135–1154.

Pichon, X. L., C. Kreemer, and N. Chamot-Rooke (2005), Asymmetry in elastic properties and the evolution of large continental strike-slip faults, *J. Geophys. Res.*, **110**, B03,405, doi:10.1029/2004JB003343.

Roeloffs, E., and J. Langbein (1994), The earthquake prediction experiment at Parkfield, California, *Rev. Geophys.*, **32**, 315–336.

Schmalzle, G., T. H. Dixon, R. Malservisi, and R. Govers (2006), Strain accumulation across the Carrizo segment of the San Andreas Fault, California: Impact of laterally varying crustal properties, *J. Geophys. Res.*, **111**, B05,403, doi:10.1029/2005JB003843.

Segall, P., and R. Harris (1987), Earthquake deformation cycle on the San Andreas fault near Parkfield, California, *J. Geophys. Res.*, **92**, 10,511–10,525.

Sieh, K. E. (1978a), Central California foreshocks of the great 1857 earthquake, *Bull. Seismol. Soc. Am.*, **68**, 1731–1749.

Sieh, K. E. (1978b), Slip along the San Andreas Fault associated with the great 1857 earthquake, *Bull. Seismol. Soc. Am.*, **68**, 1421–1447.

Simpson, R., M. Barall, J. Langbein, J. Murray, and M. Rymer (2006), San Andreas fault geometry in the Parkfield, California, region, *Bull. Seismol. Soc. Am.*, **96**, S28–S37, doi: 10.1785/0120050824.

Titus, S. J., C. DeMets, and B. Tikoff (2006), Thirty-five-year creep rates for the creeping segment of the San Andreas fault and the effects of the 2004 Parkfield earthquake: Constraints from alignment arrays, continuous Global Positioning System, and creepmeters, *Bull. Seismol. Soc. Am.*, **96**, S250–S268.

Titus, S. J., M. Dyson, C. DeMets, B. Tikoff, F. Rolandone, and R. Burgmann (2011), Geologic versus geodetic deformation adjacent to the San Andreas fault, central California, *Geol. Soc. Am. Bull.*, **123**, 794–820, doi:10.1130/B30150.1.

Toke, N. A., and J. R. Arrowsmith (2006), Reassessment of a slip budget along the Parkfield segment of the San Andreas fault, *Bull. Seismol. Soc. Am.*, **96**, S339–S348.

Toke, N. A., J. R. Arrowsmith, J. J. Young, and C. J. Crosby (2006), Paleoseismic and postseismic observations of surface slip along the Parkfield segment of the San Andreas fault, *Bull. Seismol. Soc. Am.*, **96**, S221–S238.

Wyatt, F. K., and D. C. Agnew (2004), The PIN1 and PIN2 GPS Sites at Piñon Flat Observatory, *Sio technical report*, Scripps Institution of Oceanography, available at `http://escholarship.org/uc/sio_techreport`.